

Density functional calculations of atomic structure, charging effect, and static dielectric constant of two-dimensional systems based on B-splines

Chung-Yuan Ren^{a,†} and Yia-Chung Chang^{b,c}

^a *Department of Physics, National Kaohsiung Normal University, Kaohsiung 824, Taiwan*

^b *Research Center for Applied Sciences,
Academia Sinica, Taipei 115, Taiwan*

^c *Department of Physics, National Cheng-Kung University, Tainan 701, Taiwan*

† *E-mail address: cyren@ncku.edu.tw*

Abstract

We implement a total-energy minimization scheme to allow for relaxation of atomic positions in density functional calculations for two-dimensional (2D) systems using a mixed basis set. The basis functions consist of products of 2D plane waves in the plane of the material and localized B-splines along the perpendicular direction. By using this mixed basis approach (MBA), we studied the atomic relaxation and charge polarization of 2D systems under an applied electric field. Compared to the conventional supercell approach (SCA) which adopts repeated slabs sandwiched between vacuum regions, MBA makes no requirement of compensating background charge for treating electrically charged 2D systems due to carrier injection. Furthermore, with MBA, the sawtooth potentials for systems under the applied field to maintain periodicity as needed in SCA is automatically avoided. From the linear response of charge polarization to the applied field, we introduced a simple method to determine the out-of-plane dielectric constants of 2D materials without the ambiguity of defining their effective thickness. Selected 2D systems including graphene and transition-metal dichalcogenides are tested. Our MBA results are consistent with previous SCA calculations when both approaches are equally applicable. However, for the charged system with high carrier density, we found significant deviation from SCA results obtained by imposing artificial charge neutrality condition.

PACS: 71.15.Mb, 73.20.-r

I. INTRODUCTION

It is well known that the electronic properties of low-dimensional systems are fundamentally different from those in higher dimensions due to their unusual collective excitations. Two-dimensional (2D) nano-materials can be easily fabricated because of the emerging nanotechnology and have been attracting much attention in fields of both theoretical and applied science for material innovation.

First-principles methods based on density functional theory (DFT) with pseudopotential (PP) scheme have been used widely in the electronic structure calculations of solid-state physics and quantum chemistry. In many calculations, three-dimensional (3D) plane waves (PW) are used as basis functions, which are suitable for bulk systems. Because PWs are easily implemented, not atom-centered, and can systematically achieve convergence, they are often employed to expand the wavefunction even along the non-periodic direction in 2D systems by the supercell approach (SCA). In this respect, the physical 2D system is treated as a fully 3D periodic system by introducing artificial vacuum space to separate the repeated slabs along the direction, which should be considered as nonperiodic. However, SCA requires large enough thickness of the vacuum layer such that the interactions between the adjacent slabs are negligible, and therefore increases the number of PW along that direction.

More seriously, for electrically charged systems (or systems with charged defects), the long-range tail of the Coulomb potential inevitably requires an extremely large separation of the two slabs and makes the calculation impractical. This would even cause the convergence problem due to the infinitely periodic array of charged defects, no matter how large the unit cell was chosen. One simple way to avoid this issue is the use of charge neutrality condition by adding an additional compensating charge to make the whole system electrically neutral. Several more sophisticated correction schemes have also been devised to remedy the difficulty [1]-[6]. Another drawback of SCA is the unavoidable discontinuity of the sawtooth potential in the system under an external E-field [7, 8] or an asymmetric slab with a net surface dipole density (like ferroelectric BaTiO₃) [7]. Such discontinuity still persists with the proposed dipole correction [8] and should be placed within the vacuum region, where physical quantities of interest are ensured to be negligible.

In previous work [9]-[12], a mixed basis approach (MBA) has been introduced for the first-principles calculations of low-dimensional systems by expanding the wavefunction along the

periodic direction with PW but along the finite non-periodic direction with localized basis functions. MBA uses only one slab that contains the physical atom layers and some nearby vacuum space to allocate BS basis functions. MBA has several advantages over SCA: (1) In MBA, each unit cell corresponds to the true unit cell of the real 2D material. MBA retains the layer-like local geometry as in the real physical surfaces. (2) Instead of using alternating slabs and vacuum regions in SCA, one can directly calculate the energetics, structure, and dynamics of an isolated slab without any correction. (3) For charged systems, the spurious Coulomb interaction between the excess charge, its images and the compensating background charge in SCA can be automatically avoided. (4) In an external electric field or with surface dipole moments, MBA needs no inclusion of dipole-corrected slabs. (5) The number of the basis could be reduced, easing the computational burden for the diagonalization of the Kohn-Sham Hamiltonian. MBA, conceptually very simple, is suitable for investigating low-dimensional systems including surfaces, interfaces, and superlattices.

As demonstrated elsewhere[11]-[15], B-splines (BSs) are well suited to describe the localized wavefunction. We choose BS as the basis in MBA to expand the Kohn-Sham orbitals perpendicular to the surface. BSs are highly localized piecewise polynomials within prescribed break points. BS has several desired properties: (1) BSs and their derivatives can be evaluated easily and precisely. (2) BSs possess good flexibility to represent a rapidly varying wavefunction accurately by adjusting the break points to have an optimized basis. (3) Unlike Gaussian functions and atomic orbitals which are an atom-centered basis, BSs are independent of atomic positions [16, 17], so the atomic-structure optimization can be implemented without complexity.

We notice that one B-spline-based finite-element (FE) approach was developed to achieve chemical accuracy efficiently [18]. FE avoids transformation into the reciprocal space and its numerical efforts are linear with the system size [19]. Such approach has proven to be efficient for polyatomic molecules/clusters and allows for more flexible boundary conditions to the solution of Poisson equation [20]-[22] (an overview of FE can be found in Refs. [18, 19, 23]). Therefore, our MBA-BS, with local discretization refinement embedded in FE, would be beneficial to one dimensional systems (e.g. an infinitely long graphene nanoribbon) where the real-space integration involves two non-periodic directions.

In this paper, based on DFT with Vanderbilt's ultra-soft pseudopotential (USPP) [24], we extend our previous MBA approach [11] to study the atomic and electronic structures

of selected 2D systems, particularly for charged systems and systems under an applied E-field. We examine the atomic relaxation, the charging effect due to carrier injection, and the static dielectric constant within the MBA-BS scheme. This paper is organized as follows: In Sec. II, the computational method is presented. In Sec. III, we report the results of practical tests, which demonstrate explicitly the MBA capability. The results are displayed and discussed. Finally, the summary is given in Sec. IV. The relevant details of the total energy and force formula in terms of BS for 2D systems are shown in the Appendix.

II. METHOD OF CALCULATION

A. B-splines

For the sake of completeness, we briefly summarize the BS formalism. More details can be found in Refs. [11, 25].

BSs of order κ , $\{B_{i,\kappa}(z)\}_{i=1,\dots}$, are determined by a sequence of nondecreasing numbers $\{\tau\}$ which is referred to as a knot sequence. $\{B_{i,\kappa}(z)\}$ is a set of locally positive polynomials of degree $\kappa - 1$ with compact support $\tau_i \leq z \leq \tau_{i+\kappa}$ and vanish everywhere outside those subintervals.

BS is generated by the recursive relation :

$$B_{i,\kappa}(z) = \frac{z - \tau_i}{\tau_{i+\kappa-1} - \tau_i} B_{i,\kappa-1}(z) + \frac{\tau_{i+\kappa} - z}{\tau_{i+\kappa} - \tau_{i+1}} B_{i+1,\kappa-1}(z), \quad (1)$$

with

$$B_{i,1}(z) = \begin{cases} 1, & \tau_i \leq z < \tau_{i+1} \\ 0, & \text{otherwise} . \end{cases} \quad (2)$$

Its first derivative is given by

$$\frac{d}{dz} B_{i,\kappa}(z) = \frac{\kappa - 1}{\tau_{i+\kappa-1} - \tau_i} B_{i,\kappa-1}(z) - \frac{\kappa - 1}{\tau_{i+\kappa} - \tau_{i+1}} B_{i+1,\kappa-1}(z). \quad (3)$$

Therefore, the derivative of BSs of order κ is simply a linear combination of BS of order $\kappa - 1$, which is also a simple polynomial and is continuous across the knot sequence. The flexibility of BS to accurately represent localized functions was demonstrated in Ref. [11].

In practical calculations, we use $\kappa = 4$, that is, BSs are cubic polynomials.

B. Hamiltonian and total energy

Atomic units, $m = \hbar = e = 1$, are used throughout this paper.

With BS for the non-periodic z direction and 2D PW for the periodic xy plane, the mixed basis used to expand the wavefunction is defined as

$$\langle \mathbf{r} | \mathbf{k} + \mathbf{g}; j, \kappa \rangle = \frac{1}{\sqrt{A}} e^{i(\mathbf{k}+\mathbf{g})\cdot\rho} B_{j,\kappa}(z), \quad (4)$$

where \mathbf{g} denotes 2D reciprocal lattice vector and \mathbf{k} is Bloch wave vector. A is the surface area of the system. Therefore, the charge density can be written in the form

$$n(\mathbf{r}) = \sum_{\mathbf{g}} n(\mathbf{g}, z) e^{i\mathbf{g}\cdot\rho}, \quad (5)$$

where the sum runs over up to an appropriate energy cutoff.

In USPP scheme [24, 26], the wave function ϕ_i satisfies a secular equation of the form

$$H|\phi_i \rangle = \epsilon_i S|\phi_i \rangle, \quad (6)$$

subject to a generalized orthonormality condition

$$\langle \phi_i | S | \phi_j \rangle = \delta_{ij}. \quad (7)$$

Here,

$$H = -\frac{1}{2}\nabla^2 + V_{\text{eff}} + \sum_{Inm} D_{nm}^I |\beta_n^I \rangle \langle \beta_m^I|. \quad (8)$$

The screened effective local potential V_{eff} includes the local potential part of USPP, Hartree potential, and exchange-correlation potential,

$$V_{\text{eff}} = V_{\text{loc}} + V_H + v_{xc}. \quad (9)$$

The last term of the right hand side in Eq. (8) is the non-local potential part V_{NL} of USPP and β_n^I is the n^{th} projector function, centered on site I .

As for the overlap operator S , it is given by

$$S = 1 + \sum_{Inm} q_{nm}^I |\beta_n^I \rangle \langle \beta_m^I|, \quad (10)$$

where $q_{nm}^I = \int d\mathbf{r} Q_{nm}^I(\mathbf{r})$. The augmentation functions $Q_{nm}^I(\mathbf{r})$, also centered on site I , are strictly localized in core regions. Note that D_{nm}^I in Eq. (8) should be determined self-consistently via

$$D_{nm}^I = D_{nm}^0 + \int d\mathbf{r} Q_{nm}^I(\mathbf{r}) V_{\text{eff}}(\mathbf{r}), \quad (11)$$

where the strength D_{nm}^0 is provided by USPP and differs for different ion species. The charge density from the wave function is augmented inside the core region,

$$n(\mathbf{r}) = \sum_i |\phi_i(\mathbf{r})|^2 + \sum_{Inmi} Q_{nm}^I(\mathbf{r}) \langle \phi_i | \beta_n^I \rangle \langle \beta_m^I | \phi_i \rangle. \quad (12)$$

The total energy E_{tot} is given by

$$E_{tot} = \sum_i w_i \langle \phi_i | H | \phi_i \rangle - \frac{1}{2} \int d\mathbf{r} n(\mathbf{r}) V_H(\mathbf{r}) - \int d\mathbf{r} n(\mathbf{r}) v_{xc}(\mathbf{r}) + E_{xc} + E_{ii}, \quad (13)$$

where the sum runs over the occupied states with appropriate weight w_i . Here, $E_{xc} = \int d\mathbf{r} (n + n_c) \varepsilon_{xc}[n + n_c]$ is the exchange-correlation energy with pseudized core charge density n_c if nonlinear core correction (NLCC) [27] is taken into account. E_{ii} denotes the ion-ion repulsive energy. When an external electric field $\mathbf{E} = \mathcal{E}_0 \hat{\mathbf{e}}_z$ perpendicular to the surface is applied, E_{tot} in Eq. (13) is added with

$$E_E = \int d\mathbf{r} n(\mathbf{r}) V_E(z) - \mathcal{E}_0 \sum_I Z_I z_I. \quad (14)$$

where $V_E(z) = -\mathcal{E}_0 z$. Z_I and z_I are the ionic charge and z -coordinate of ion I , respectively.

C. Force

The forces are defined as the total derivative of the total energy with respect to ionic positions \mathbf{R}_I ,

$$\mathbf{F} = -\frac{dE_{tot}}{d\mathbf{R}_I}. \quad (15)$$

To demonstrate the flexibility of BSs, we only focus on the z -component.

Using Hellmann-Feynman theory, the force within USPP scheme is

$$F_z = -\sum_i w_i \langle \phi_i | \frac{\partial(H - \epsilon_i S)}{\partial z_I} | \phi_i \rangle - \frac{\partial E_{xc}}{\partial z_I} - \frac{\partial E_{ii}}{\partial z_I}. \quad (16)$$

Note that we need not to calculate the change of V_H or v_{xc} in H due to the change of the soft or the augmented charge because, to the first-order, the change of the sum of Kohn-Sham eigenvalues will cancel out the change of these potential contributions [28]. It turns out that there are several contributions to the total force. The first term is

$$F_{Iz}^{loc} = -\int d\mathbf{r} n(\mathbf{r}) \frac{\partial V_{loc}(\mathbf{r})}{\partial z_I}. \quad (17)$$

The second term arises from D_{mn} due to the change of the augmentation charge when the ion is moving,

$$F_{Iz}^{ln,1} = - \sum_{nmi} \left[\int d\mathbf{r} \frac{\partial Q_{nm}^I(\mathbf{r})}{\partial z_I} V_{\text{eff}}(\mathbf{r}) \right] \omega_i \langle \phi_i | \beta_n^I \rangle \langle \beta_m^I | \phi_i \rangle. \quad (18)$$

The third one is due to the change of the projector and is given by

$$F_{Iz}^{ln,2} = - \sum_{nmi} \omega_i (D_{nm}^I - q_{nm}^I \epsilon_i) \langle \phi_i | \frac{\partial |\beta_n^I\rangle \langle \beta_m^I|}{\partial z_I} | \phi_i \rangle \quad (19)$$

In the $-\partial E_{xc}/\partial z_I$ term in Eq. (16), the force due to the change of the frozen pseudized core charge n_c is

$$F_{Iz}^{nlcc} = - \int d\mathbf{r} v_{xc}(\mathbf{r}) \frac{\partial n_c^I(\mathbf{r})}{\partial z_I}. \quad (20)$$

The ion-ion force can be treated by the Ewald sum [29, 30]. The detailed mathematical derivations of the relevant force components, as well as $H(S)|\phi_i\rangle$ based on MBA-BS for 2D systems will be given in the Appendix.

We used the conjugate-gradient algorithm implemented previously [32] for the eigenvector/eigenvalue searching. The geometry optimization was performed with the Broyden-Fletcher-Goldfarb-Shanno (BFGS) algorithm [31] to find the total energy minimum.

D. No charge neutrality condition

The electrostatic potential V_c in 2D momentum representation is

$$V_c(\mathbf{g} \neq 0, z) = \int dz' n_t(\mathbf{g}, z') \frac{2\pi}{|\mathbf{g}|} e^{-|\mathbf{g}||z-z'|}. \quad (21)$$

Here, n_t consists of electron and ion charge density.

For $|\mathbf{g}| \rightarrow 0$,

$$\begin{aligned} V_c(\mathbf{0}, z) &= \int dz' n_t(\mathbf{0}, z') \frac{2\pi}{|\mathbf{g}|} (1 - |\mathbf{g}||z-z'|) \\ &= \frac{2\pi}{|\mathbf{g}|} \int dz' n_t(\mathbf{0}, z') - 2\pi \int dz' n_t(\mathbf{0}, z') |z-z'| \end{aligned} \quad (22)$$

The first term of the right hand side in the above equation could be safely dropped if the system is charge neutral. For the situation of nonzero net charge, the $V_c(\mathbf{0}, z)$ component is rewritten as

$$\begin{aligned} V_c(\mathbf{0}, z) &= \iiint dz' \frac{d^2 \rho'}{\sqrt{\Delta z^2 + \rho'^2}} n_t(\mathbf{0}, z') \\ &= \iint_0^R dz' \frac{2\pi \rho' d\rho'}{\sqrt{\Delta z^2 + \rho'^2}} n_t(\mathbf{0}, z'), \end{aligned} \quad (23)$$

where we assume R , the 'radius' of the system along the xy plane be arbitrarily large but finite, and $\Delta z = z - z'$. Since R is much larger than the dimensional size in the z direction, i.e., $R \gg \Delta z$, then

$$\int_0^R \frac{\rho' d\rho'}{\sqrt{\Delta z^2 + \rho'^2}} = \sqrt{R^2 + \Delta z^2} - |\Delta z|$$

$$\sim R - |\Delta z|. \quad (24)$$

So,

$$V_c(\mathbf{0}, z) = 2\pi R \int dz' n_t(\mathbf{0}, z') - 2\pi \int dz' n_t(\mathbf{0}, z') |z - z'|. \quad (25)$$

In the case of charge neutrality, the first term on the right hand side of Eq. (25) vanishes and we retain Eq. (22). For charged systems with net planar charge density $\int dz' n_t(\mathbf{0}, z') \neq 0$, such term would be huge. But clearly it is a constant that is independent upon z , and only causes a shift to the total energy. This kind of constant is irrelevant to the band structure calculation. Therefore, we could, just like the charge-neutral case, omit the first term without further corrections. What we need to care about is only the second term on the right hand side of Eq. (22) for both neutral and charged cases within MBA.

III. APPLICATIONS OF PRESENT METHOD

A. Preliminary numerical test

First of all, we take 2H MoS₂ monolayer to test the MBA performance. In the 2H phase, Mo occupies at the Wykoff 1c site (0, 0, 0) and S occupies at the 2s sites (1/3, 2/3, $\pm u$). We perform total energy calculations to find the relaxed internal coordinate u . The in-plane lattice constant a_0 was set to 3.16 Å. The calculations were done with 25 BSs that are distributed over a range of 4.0 a_0 and the energy cutoff of 20 Ry for 2D PW. A Monkhorst-Pack 7×7 mesh including Γ point was taken to sample the 2D irreducible Brillouin zone (IBZ). We used Mo and S USPPs [24, 33] which were generated from the Vanderbilt's code [34]. The generalized gradient approximation with Perdew-Burke-Ernzerhof exchange-correlation functional [35] is adopted. The potential is determined self-consistently until its change is less than 10^{-7} Ry.

Figure 1 shows E_{tot} as a function of u , with the change in steps of $\Delta u \sim 0.001$ near the minimum. The energy in this figure is given relative to some reference energy. The energy minimum occurs around $u = 0.497$, which is very close to the value of 0.4972 by the BFGS algorithm. The residual force along z direction is found to be less than 0.01 mRy/a.u.

We also summarize in Table I the relevant information for the total number of basis functions used by both MBA and SCA. It is worth mentioning that the range of vacuum space in MBA are mainly determined by the wavefunction, which quickly decays outside the surface (at least for electrically neutral and positively charged systems). On the other hand, the vacuum layers in SCA depend upon the Coulomb potential which could exhibit a long-range tail in the vacuum space. The reduction in the number of basis by MBA will ease the computational efforts for the Kohn-Sham eigenvalue searching, which is the dominant cost in DFT calculations. We found that the execution time for the self-consistent loop by the present code is 5.3 seconds per iteration per processor, compared to the 1.9 seconds by VASP which is well developed and optimized with 3D plane waves. Needless to say, the comparison for the running time will depend on the size of vacuum space set in VASP, the real-space grids for FFT, the quality of pseudo-potentials (like the number of projectors) and the algorithms used. For example, the time is found to be 2.6 seconds per iteration per processor with an increasing vacuum layer of 15 Å in VASP.

In this work, we do not intend to compete in speed with the planewave-based codes. The advantages of MBA mentioned in the Introduction will come at the price of extra real-space integration along the perpendicular direction. Maybe other methodologies, e.g., the 3D BS-FE approach [18] could be studied in the future. The data presented here are just to give an idea of how our MBA works in speed with respect to VASP. In any case, the real-space integration is computationally moderate because of the characteristics of the smoothness of USPP. In addition, relevant quantities with the integration can be precalculated to speed up the calculation in the self-consistent iteration loop.

B. Transition Metal Dichalcogenides

Now, we systematically performed structural optimization for transition metal dichalcogenides (TMDC) MX_2 , which have attracted much attention recently [36]. TMDC are characterized by their layered structures. Here, we study the electronic and structural properties of two monolayer MX_2 families: MoS_2 family with $\text{M}=\text{Mo}$, W and $\text{X}=\text{S}$, Se , and ZrS_2 family with $\text{M}=\text{Zr}$, Hf and $\text{X}=\text{S}$, Se . We focus on the 2H phase only and carry out the optimization of u with experimental lattice constants [37]-[41]. The calculation condition is similar to that in the above preliminary test. For the ZrS_2 family, the BS number is slightly increased to 29 to account for the larger size. For comparison, we also performed calculations by SCA implemented in the VASP code with projector-augmented-wave (PAW) potentials [28, 42]. A typical vacuum space of 10-15 Å required in VASP was used in the calculation.

Table II summarizes the optimized vertical M-X distance d_z (ua_0) and band gap E_g of these eight compounds, along with those obtained by VASP. Overall, we found a good agreement between the present d_z results and those by VASP. We also examine with another two different BS sets and d_z is almost unaltered.

As for the electronic structure, we display the band structures of MoS_2 and ZrS_2 in Figs. 2(a) and (b) for the two families. Figures 2(c) and (d) show the corresponding VASP counterparts. Clearly, MoS_2 has a direct band gap with both valence band maximum and conduction band minimum falling at K ($\mathbf{k}=(1/3,1/3)$) whereas ZrS_2 has an indirect band gap, which agree well between MBA and SCA. A detailed analysis shows that, for ZrS_2 , valence band maximum occurs within segment K- Γ , and conduction band minimum falls within segment Γ -M ($\mathbf{k} = (1/2, 0)$), It can be seen from Table I that E_g obtained by MBA

is in a quantitative agreement with the VASP result. The only slight discrepancy which appears in the HfS₂ and HfSe₂ cases is attributed to the quality of Hf pseudopotentials used. Actually, we have done the calculation with two different Hf USPPs (and PAWs) and found that while the optimized d_z is almost unaffected, E_g differs significantly (~ 0.15 eV), reflecting the sensitivity of the electronic structure to Hf PP quality.

C. Charged graphene

Next, we apply the present method to electrically charged systems which are very challenging for SCA because of the spurious long-range Coulomb interaction between the excess charge and its periodic images due to the periodic boundary condition [43]. Naturally, it should remove such boundary condition to study the surfaces that are charged up or have dipole moments. Charged 2D systems can be achieved experimentally via carrier injection in a field-effect-transistor setup [44].

For simplicity, we use the graphene sheet as a test example. All carbon atoms were kept at ideal positions with $a_0 = 2.46$ Å. Here, one of every eight valence electrons in the unit cell was removed, that is, the nominal ionicity of C in this artificial positively-charged system is +0.5. 13 BSs distributed over a range of $3.25 a_0$ are used and the energy cutoff of the 2D PW is 30 Ry. A dense Monkhorst-Pack 21×21 mesh was used to sample the surface IBZ of this metallic system.

The calculated band structure is shown in Fig. 3(a). For comparison, we also do the calculation imposed by the charge neutrality condition with a compensating charge. The corresponding result is presented in Fig. 3(b) and the VASP counterpart in Fig. 3(c). Clearly, with charge neutrality condition, MBA yields similar band structures with the VASP. However, the results with and without charge neutrality condition are significantly different [45], particularly those near Fermi level around Γ point.

In SCA, the charged defects are unfortunately subjected to the spurious image interaction, and no feasible size in practice would be sufficient to render this long-ranged electrostatic interaction negligible. A cheap way to avoid divergence of the electrostatic energy is to impose an additional compensating charge into the system. In some experiments, the surrounding medium (like metal or solution) around these excess charges would change its electron spatial distribution to perfectly screen the defects so that the the above imposition

was justified [43]. However, in some situations, the 'reference' electrode is put sufficiently far away from the system interested, for example, the charged surface of the Van de Graaff sphere or the rubbed plastic plate with a net static electricity. The often imposed charge neutrality condition would not be valid.

It's true that the Coulomb potential would diverge even along an infinitely ideal charged plane. But, actually in reality all physics systems are finite, e.g., the rubbed plastic plate. How can we investigate such a system? Clearly, with the size of planar charged systems being arbitrarily large but *finite*, the first term in Eq. (22) or (25) can be safely dropped out, as explained in Section IID, and our method can be used to mimic this kind of systems except for the edge effect. All we have to do is to evaluate the second term of Eq. (22) no matter the system has an excess charge or not. No further corrections are needed in MBA since only one single isolated charged slab rather than an array of the replicated ones is under consideration.

The key point of the present method is the utility of Eq. (21) for Coulomb potential for 2D systems instead of the usual expression of $\sim n_t(\mathbf{G})/|\mathbf{G}|^2$ for 3D systems (\mathbf{G} denotes a 3D reciprocal lattice vector). It may be argued that the large constant in the first term of Eq. (25) can also be dropped in the 3D plane-wave code without affecting the relative band energies. However, to evaluate the second term in Eq. (25), some remedy will be required to subtract the artificial contributions generated from periodically repeated charged sheets included in the 3D supercell method.

Note that the convergence rate of the calculation is stable and as fast as for the neutral case, as shown in Fig. 4. To our knowledge, it seems that the existing packages based on SCA could not deal with such situation where the charge neutrality condition was unsatisfied. MBA provides an alternative way to study both neutral and charged 2D systems with no complications.

D. Bilayer graphene under an external \mathbf{E} field

The third example is the system of bilayer graphene under an external E-field, as shown in Fig. 5(a). All atoms in the graphene sheets were kept at ideal positions. The in-plane lattice constant a_0 is 2.46 Å, and the inter-plane distance d is 3.35 Å[46]. A mixed basis set with 23 BSs over a range of 5.0 a_0 and 2D PW with an energy cutoff of 30 Ry was used to

expand the wavefunction.

In the absence of the electric field, bilayer graphene is a gapless semiconductor. Previous works [47, 48] with a tight-binding model have reported that the application of an external electric field to the bilayer system with AB-stacking lifts the degenerate states at K to form the so-called Mexican-hat-like band structure. The field-induced energy gap occurs not at K but slightly away from it. This means that a more dense k -point sampling near K valley is required to ensure the calculation convergence. Here, instead of a uniform division, we use a non-uniform k -point distribution, as demonstrated in Fig. 5(b). In essence, there are three zones of different sampling density in the BZ, with denser sampling near K point. For clarity, we denoted the division in Fig. 5(b) as $3 \times 3 \times 3$. We found that the sampling with $12 \times 6 \times 6$ division leads to excellent convergence. This corresponds to only 31 k -points in IBZ, as compared to 184 points by the uniform 44×44 Monkhorst-Pack division used in literature [49].

To compare with the earlier DFT calculation [46], we change the strength \mathcal{E}_0 such that the parameter $U_{ext} = \mathcal{E}_0 d$ is 0, 0.5, 1.0, and 1.5 eV. The band structures of these four cases near K valley (along fragment of Γ -K-M) are shown in Fig. 6. Clearly, the gap increases with increasing U_{ext} . It is found that a nice agreement with previous results [46] was obtained. This agreement confirms that our MBA successfully captures the above characters of the complicated band structure near Fermi level at K valley.

E. Dielectric constant of MS_2 (M=Mo, Zr) under an external E-field

Finally, we studied the out-of plane static dielectric constant of 2D TMDC under an external electric field. The electronic property of MoS_2 is influenced by atomic structure and can be controlled by various ways [50]-[52]. Layered MoS_2 has been considered a promising candidate for the post-silicon-era field-effect-transistor [53]. We select MoS_2 and ZrS_2 to study the field-induced dipole moment of their monolayer (1L) and bilayer (2L) to simulate the influence of the gate voltage upon such nanoelectronic devices.

The z -coordinate of all ions was allowed to relax. The Van der Waals interlayer interactions were taken into account with Grimme's DFT-D2 version [54] to correct the total energy and force. The energy cutoff of 2D PW was increased to 40 Ry. There are 45 BSs over a range of $6a_0$ for the 2L case. In addition, the amplitude \mathcal{E}_0 is chosen such that the

electrostatic potential V_E at the edge region in the z direction is higher than the Fermi level to avoid unwanted charge transfer from the surface to the edge. To compare with the literature [55], 2H MoS₂ stacking in A-B order and 1T ZrS₂ in A-A order for the 2L case are considered. Here, for the 1T phase, the two S atoms in one unit cell occupy at the sites $(1/3, 2/3, u)$ and $(2/3, 1/3, -u)$. The surface k -point sampling is the same with the first example.

The polarized layered structure exhibits a net electric dipole moment m in response to the external E-field,

$$m = \int dz \bar{n}_{scr}(z) z, \quad (26)$$

where \bar{n}_{scr} is the screening planar-averaged total charge density (including the electronic and ion contributions),

$$\bar{n}_{scr}(z) = \frac{1}{A} \int d\boldsymbol{\rho} (n_E(\mathbf{r}) - n_0(\mathbf{r})), \quad (27)$$

with n_E and n_0 being respectively the charge density with and without the external field. We checked the calculations for the 1L MoS₂ case with various \mathcal{E}_0 and found that m changes linearly in \mathcal{E}_0 , as expected.

The static dielectric constant ϵ_0 was calculated via

$$\epsilon_0 = \frac{\mathcal{E}_0}{\mathcal{E}_0 - 4\pi P}. \quad (28)$$

The average polarization P here was deduced from m/t [7] where t is the effective thickness of the layers interested. Obviously, the dielectric constant is sensitive to the thickness chosen. For example, when we use the thickness suggested in Ref. [55], the dielectric constant of 1L and 2L MoS₂ is respectively, 6.2 and 6.8. But, if the thickness were chosen as the distance between the center of gravity of the screening charge distribution of the top and bottom charge layers suggested in Ref. [7] (also shown in Fig. 7), then these values become 38.9 and 10.4, respectively.

Table III summarizes the calculated dielectric constant and the thickness used. These results were evaluated based upon $\mathcal{E}_0 = 0.005$ a.u.. Since the dielectric constant can be rescaled for different values of thickness, we also present the value of m as the base for calculations. It is clear that the dielectric constant obtained with the thickness from Ref. [55] is in agreement with that work [55]. So, our approach can directly calculate the dielectric through Eq. (28) without the correction due to the existence of vacuum spaces needed in SCA [49, 55].

To avoid ambiguity in the dielectric constant with the choice of thickness, we address this issue from another approach. In analog with the atomic Stark effect, the external E-field can significantly modulate the band gap of bilayer graphene and TMDC [56]-[59]. This indicates that the change of the band gap could reflect information of the screened electric field inside the bilayer system, which is the central point in calculating the dielectric constant. Based on this observation, we suppose that the reduction in the gap from the $\mathcal{E}_0 = 0$ case is approximately linear to the amount of the net electric field strength. In this respect, we additionally performed a non-self-consistent calculation of the gap difference $\Delta E_{g,nsclf}$ under the external E-field by keeping the charge density n_0 unchanged as at zero field. Together with the gap difference $\Delta E_{g,scf}$ obtained by using the self-consistent charge density n_E in response to the E-field, we can estimate the dielectric constant as the ratio of $\Delta E_{g,nsclf}$ to $\Delta E_{g,scf}$. Through this scenario, the dielectric constant of 2L MoS₂ and ZrS₂ is found to be 9.0 and 4.5, respectively, comparable to the values of 10.4 and 5.1 in Table II obtained with the thickness suggested in Ref. [7]. Therefore, the use of such a ratio could reasonably determine the dielectric constant and it does not depend on the effective thickness t .

IV. CONCLUSIONS

In conclusion, we have successfully implemented MBA to investigate the atomic and electronic structures of 2D systems by expanding the wavefunctions with PW for the periodic directions and BS for the non-periodic direction. Contrary to the existing algorithms based upon SCA with repeated slabs embedded in vacuum regions, MBA is a real space approach along the non-periodic direction. For charged systems due to carrier injection, the spurious Coulomb interaction between the carrier, its images and the compensating background charge by SCA is avoided in MBA. Moreover, we can directly study the charge polarization of the system influenced under an external E-field with no potential discontinuity that appears in SCA. The localized BS has proved to be flexible for expanding the out-of-plane wavefunction during geometry optimizations. Our MBA results for the atomic relaxation and dielectric constant under the applied E-field are consistent with SCA calculations when both approaches are equally applicable. However, it is found that SCA is no longer valid for treating the charged system with high carrier density by imposing artificial charge neutrality condition. We believe that MBA-BS is suitable for investigating more realistic 2D materials.

Acknowledgments

This work was supported by Ministry of Science and Technology under grant numbers MOST 108-2112-M-017 -001 and MOST 108-2112-M-001-041 and by National Center for Theoretical Sciences of Taiwan.

-
- [1] S. E. Taylor and F. Bruneval, Phys. Rev. B **84**, 075155 (2011), and references therein.
 - [2] G. Makov and M. C. Payne, Phys. Rev. B **51**, 4014 (1995).
 - [3] C. A. Rozzi, D. Varsano, A. Marini, E. K. U. Gross, and A. Rubio, Phys. Rev. B **73**, 205119 (2006).
 - [4] N. D. M. Hine, J. Dziedzic, P. D. Haynes, and C. K. Skylaris, J. Chem. Phys., **135**, 204103 (2011).
 - [5] R. Sundararaman, , K. Letchworth-Weaver, K. A. Schwarz, D. Gunceler, Y. Ozhabes, and T. A. Arias, SoftwareX, 6, 278 (2017).
 - [6] S. Ismail-Beigi, Phys. Rev. B **73**, 233103 (2006).
 - [7] B. Meyer and D. Vanderbilt, Phys. Rev. B **63**, 205426 (2001).
 - [8] L. Bengtsson, Phys. Rev. B **59**, 12301 (1999).
 - [9] G.-W. Li and Y.-C. Chang, Phys. Rev. B **48**, 12032 (1993).
 - [10] G.-W. Li and Y.-C. Chang, Phys. Rev. B **50**, 8675 (1994).
 - [11] C. Y. Ren, C. S. Hsue and Y.-C. Chang, Comp. Phys. Comm. **188**, 94 (2015).
 - [12] C. Y. Ren, Y.-C. Chang, and C. S. Hsue, Comp. Phys. Comm. **202**, 188 (2016).
 - [13] W. R. Johnson, S. A. Blundell, and J. Sapirstein, Phys. Rev. A **37**, 307 (1988).
 - [14] H. T. Jeng, and C. S. Hsue, Phys. Rev. B **62**, 9876 (2000).
 - [15] C. Y. Ren, H. T. Jeng, and C. S. Hsue, Phys. Rev. B **66**, 125105 (2002).
 - [16] D. Alfè and M. J. Gillan. Phys. Rev. B **70**, 161101(R) (2004).
 - [17] E. Hernández, M. J. Gillan, and C. M. Goringe, Phys. Rev. B **55**, 13485 (1997).
 - [18] I. Temizer, P. Motamarri, and V. Gavini, J. Comput. Phys. **241**, 112 (2020).
 - [19] S. Goedecker, Rev. Mod. Phys. **71**, 1085 (1999).
 - [20] S. R. White, J. W. Wilkins, and M. P. Teter, Phys. Rev. B **39**, 5819 (1989).
 - [21] E. Tsuchida and M. Tsukada, Phys. Rev. B **54**, 7602 (1996).

- [22] E. J. Bylaska, M. Holst, and J. H. Weare, *J. Chem. Theo. Comp.* **5**, 937 (2009).
- [23] L.R. Ram-Mohan, *Finite Element and Boundary Element Method Applications in Quantum Mechanics*, (Wiley, 2000).
- [24] D. Vanderbilt, *Phys. Rev. B* **41**, 7892 (1990).
- [25] Carl deBoor, *A practical Guide to Splines*, (Springer, New York, 1987).
- [26] K. Laasonen, A. Pasquarello, R. Car, C. Lee, and D. Vanderbilt, *Phys. Rev. B* **47**, 10142 (1993).
- [27] S. G. Louie, S. Froyen, and M. L. Cohen, *Phys. Rev. B* **26**, 1738 (1982).
- [28] G. Kresse and D. Joubert, *Phys. Rev. B* **59**, 1758 (1999).
- [29] E. Kaxiras, *Atomic and Electronic Structure of Solids*, (Cambridge, Cambridge University Press, 2003).
- [30] J. Kohanoff, *Electronic Structure Calculations for Solids and Molecules*, (Cambridge, Cambridge University Press, 2006).
- [31] We revised the subroutine `bfgs()` in *QUANTUM ESPRESSO* code:
<http://www.quantum-espresso.org>
to be compatible with our program.
- [32] C. Y. Ren, Y.-C. Chang, and C. S. Hsue, *Comp. Phys. Comm.* **238**, 138 (2019).
- [33] K. F. Garrity, J. W. Bennett, K. M. Rabe, and D. Vanderbilt, *Comp. Mater. Sci.* **81**, 446 (2014).
- [34] <http://www.physics.rutgers.edu/~dhv/uspp/> and
<http://www.physics.rutgers.edu/gbrv/>.
- [35] J. P. Perdew, K. Burke, and M. Ernzerhof, *Phys. Rev. Lett.* **77**, 3865 (1996).
- [36] H. Jiang, *J. Chem. Phys.* **134**, 204705 (2011).
- [37] B. Schonfeld, J. J. Huang, and S. C. Moss, *Acta Crystallogr.* **B39**, 404 (1983).
- [38] W. J. Schutte, J. L. de Boer, and F. Jellinek, *J. Solid State Chem.* **70**, 207 (1987).
- [39] M. K. Agarwal, P. D. Patel, and R. M. Joshi, *J. Mater. Sci. Lett.* **5**, 66 (1986).
- [40] D. L. Greenaway and R. Nitsche, *J. Phys. Chem. Solids* **26**, 1445 (1965).
- [41] D. T. Hodul and A. M. Stacy, *J. Solid State Chem.* **54**, 438 (1984).
- [42] G. Kresse and J. Furthmüller, *Comput. Mater. Sci.* **6**, 15 (1996).
- [43] M. Otani and O. Sugino, *Phys. Rev. B* **73**, 115407 (2006).
- [44] M. Sidler, P. Back, O. Cotlet, A. Srivastava, T. Fink, M. Kroner, E. Demler, and A. Imamoglu,

- Nat. Phys. **13**, 255 (2017).
- [45] In our previous work [12], the comparison between MBA and SCA for 1D charged system was made only with the charge neutrality condition.
- [46] H. Min, B. Sahu, S. K. Banerjee, and A. H. MacDonald, Phys. Rev. B **75**, 155115 (2007).
- [47] E. McCann, and V. I. Fal'ko, Phys. Rev. Lett. **96**, 086805 (2006).
- [48] E. McCann, Phys. Rev. B **74**, 161403(R) (2006).
- [49] E. J. G. Santos and E. Kaxiras, Nano Lett. **13**, 898 (2013).
- [50] J. Chang, S. Larentis, E. Tutuc, L. F. Register, and S. K. Banerjee, Appl. Phys. Lett. **104**, 141603 (2014).
- [51] J. Qi, X. Li, X. Qian, and J. Feng, Appl. Phys. Lett. **102**, 173112 (2013).
- [52] Q. Liu, L. Li, Y. Li, Z. Gao, Z. Chen, and J. Lu, J. Phys. Chem. **116**, 205325 (2011).
- [53] Y. Vaknin, R. Dagan, and Y. Rosenwaks, Nanomaterials **9**, 882 (2019).
- [54] S. Grimme, J. Comput. Chem. **27**, 1787 (2006).
- [55] A. Laturia, M. L. Van de Put, and W. G. Vandenberghe, npj 2D Mater. Appl. **2**, 6 (2018).
- [56] A. Ramasubramanian, D. Naveh, and E. Towe, Phys. Rev. B **84**, 205325 (2011).
- [57] Z. Yang and J. Ni, J. Appl. Phys. **107**, 104301 (2010).
- [58] K. H. Khoo, M. S. C. Mazzoni, and S. G. Louie, Phys. Rev. B **69**, 201401(R) (2004).
- [59] M. Ishigami, J. D. Sau, S. Aloni, M. L. Cohen, and A. Zettl, Phys. Lett. **94**, 056804 (2005).
- [60] H. Lee and W. Cai, Ewald summation for Coulomb interactions in a periodic supercell, Lecture Notes, Stanford University, 2009 (unpublished).
- [61] T. Kerber, M. Sierka, and J. Sauer, J. Comput. Chem. **29**, 2088 (2009).

V. APPENDIX I

A. construction of $H|\phi\rangle$

In MBA, we recall that the wavefunction is expanded as

$$|\phi_{\mathbf{k}}\rangle = \sum_{j\mathbf{g}} C_{j,\mathbf{k}+\mathbf{g}} |\mathbf{k} + \mathbf{g}; j, \kappa\rangle. \quad (29)$$

We will omit index \mathbf{k} in $|\phi_{\mathbf{k}}\rangle$ hereafter.

1. *kinetic energy part*

This part is given by

$$\begin{aligned}
 & -\nabla^2 |\phi\rangle \\
 & = \sum_{\mathbf{g}} \sum_{|j-j'|\leq\kappa} C_{j,\mathbf{k}+\mathbf{g}} (\langle B'_{j',\kappa} | B'_{j,\kappa} \rangle + \langle B_{j',\kappa} | B_{j,\kappa} \rangle) |\mathbf{k} + \mathbf{g}|^2 |\mathbf{k} + \mathbf{g}; j', \kappa\rangle.
 \end{aligned} \tag{30}$$

$B'_{j,\kappa}$ in Eq. (30) means the derivative of $B_{j,\kappa}$ with respect to the z coordinate.

2. *local potential part*

In practical calculations, we separate the local potential of atomic PP into a long-range potential, $V_{loc}^{at,l}(r) = -\frac{Z}{r}\text{erf}(\sqrt{a}r)$ and a short-range remainder,

$$V_{loc}^{at}(r) = V_{loc}^{at,l}(r) + V_{loc}^{at,s}(r). \tag{31}$$

The former corresponds to the potential due to an auxiliary charge distribution

$$n_a(\mathbf{r}) = \left(\frac{a}{\pi}\right)^{3/2} Z e^{-a|\mathbf{r}|^2}. \tag{32}$$

Using the fact that the 2D Fourier transform of the Coulomb potential is

$$\int dz' n_a(\mathbf{g}, z') \frac{2\pi}{|\mathbf{g}|} e^{-|\mathbf{g}||z-z'|}, \tag{33}$$

it is straightforward that the long-range part of V_{loc} in Eq. (9) in 2D momentum representation can be written as

$$\begin{aligned}
 V_{loc}^l(\mathbf{g} \neq 0, z) & = \frac{1}{A} \sum_I \frac{\pi Z_I}{|\mathbf{g}|} \left(e^{|\mathbf{g}||z-z_I|} \text{erfc}(\sqrt{a}(|z-z_I| + \frac{|\mathbf{g}|}{2a})) + e^{-|\mathbf{g}||z-z_I|} \text{erfc}(\sqrt{a}(-|z-z_I| + \frac{|\mathbf{g}|}{2a})) \right) \\
 & \quad \times e^{-i\mathbf{g}\cdot\rho_I},
 \end{aligned} \tag{34}$$

$$V_{loc}^l(\mathbf{g} = 0, z) = -\frac{1}{A} \sum_I 2\pi Z_I \left(|z-z_I| \text{erf}(\sqrt{a}|z-z_I|) + \frac{1}{\sqrt{a\pi}} e^{-a|z-z_I|^2} \right). \tag{35}$$

For the short-range part $V_{loc}^s(\mathbf{g}, z)$, we first calculate

$$V_{loc}^{at,s}(\mathbf{G}) = \int d\mathbf{r} e^{-i\mathbf{G}\cdot\mathbf{r}} V_{loc}^{at,s}(\mathbf{r}) \tag{36}$$

and

$$V_{loc}^s(\mathbf{G}) = \sum_I e^{-i\mathbf{G}\cdot\mathbf{R}_I} V_{loc}^{at,s}(\mathbf{G}). \quad (37)$$

\mathbf{G} is a compact notation for (\mathbf{g}, g_z) with $g_z = 2\pi n/L$. Here n is a integer and L is the height along z direction. It follows that $V_{loc}^s(\mathbf{g}, z)$ can be obtained by fast Fourier transform (FFT) from

$$V_{loc}^s(\mathbf{G}) = \frac{1}{L} \int dz e^{-ig_z z} V_{loc}^s(\mathbf{g}, z). \quad (38)$$

Together with the exchange-correlation potential

$$V_{xc}(\mathbf{g}, z) = \frac{1}{A} \int d\rho e^{-i\mathbf{g}\cdot\rho} V_{xc}(\mathbf{r}), \quad (39)$$

we have V_{eff} in \mathbf{g} -space representation.

3. nonlocal potential part

$Q_{nm}^I(\mathbf{g}, z)$ was calculated by analogy with the V_{loc}^s case. By knowing both $Q_{nm}^I(\mathbf{g}, z)$ and $V_{\text{eff}}(\mathbf{g}, z)$, we can update D_{nm}^I in Eq. (8) in each iteration. Furthermore,

$$\begin{aligned} & \langle \mathbf{k} + \mathbf{g}; j, \kappa | \beta^I \rangle \\ &= e^{-i(\mathbf{k}+\mathbf{g})\cdot\rho_I} \int d\mathbf{r} B_{j,\kappa}(z + z_I) e^{-i(\mathbf{k}+\mathbf{g})\cdot\rho} \beta(r) Y_{lm}(\hat{\mathbf{r}}) \\ &= \frac{2\pi}{i^m} \sqrt{\frac{(2l+1)(l-m)!}{4\pi(l+m)!}} e^{-i(\mathbf{k}+\mathbf{g})\cdot\rho_I} \int r^2 dr \sin\theta d\theta B_{j,\kappa}(r \cos\theta + z_I) J_m(|\mathbf{k} + \mathbf{g}|r \sin\theta) P_l^m(\cos\theta) \beta(r) \end{aligned} \quad (40)$$

where Y_{lm} is the spherical harmonics, P_l^m is the associated Legendre function, and J_m is Bessel function of order m . Using this one can evaluate $\langle \beta_m^I | \phi \rangle$ and therefore $V_{NL} | \phi \rangle$

$$V_{NL} | \phi \rangle = \sum_{Inm} D_{nm}^I \langle \beta_m^I | \phi \rangle | \beta_n^I \rangle. \quad (41)$$

With $H| \phi \rangle$ and $S| \phi \rangle$ in hand, we perform the eigenvalue/eigenvector searching. To speed up calculations, we expand $H| \phi \rangle / S| \phi \rangle$ as well as $| \phi \rangle$ in terms of a complementary basis $|\mathbf{k} + \mathbf{g}; j, \kappa \rangle$, where the B-splines $B_{j,\kappa}^o$ are orthogonalized (e.g. via the Grand-Schmidt procedure). Particularly, the expansion for $V_{\text{eff}}| \phi \rangle$ was obtained by 2D FFT with the computation of $\int dz V_{\text{eff}}(\boldsymbol{\rho}, z) \phi(\boldsymbol{\rho}, z) B_{j,\kappa}^o(z)$. Therefore, the vector-product performance in

the conjugate-gradient algorithm is similar to that implemented in the planewave-based codes [31, 42].

Of course, $V_E(z)$ in Eq. (14) is added to H if an external E-field is applied. In practice, the reference electric potential is set at the middle height in the z direction.

B. force:

1. component due to the local potential

From Eqs. (34) and (35), the derivative of the long-range part can be shown as

$$\begin{aligned} & \frac{\partial V_{loc}^l(\mathbf{g} \neq 0, z)}{\partial z_I} \\ &= \left\{ \frac{\pi Z_I}{A} \left(e^{|\mathbf{g}|(z-z_I)} \operatorname{erfc}\left(\sqrt{a}\left((z-z_I) + \frac{|\mathbf{g}|}{2a}\right)\right) - e^{-|\mathbf{g}|(z-z_I)} \operatorname{erfc}\left(\sqrt{a}\left(-(z-z_I) + \frac{|\mathbf{g}|}{2a}\right)\right) \right) \right. \\ & \left. + \frac{\pi Z_I}{A|\mathbf{g}|} \sqrt{a/\pi} \left(e^{|\mathbf{g}|(z-z_I)} e^{-a\left((z-z_I) + \frac{|\mathbf{g}|}{2a}\right)^2} - e^{-|\mathbf{g}|(z-z_I)} e^{-a\left(-(z-z_I) + \frac{|\mathbf{g}|}{2a}\right)^2} \right) \right\} e^{-\mathbf{g} \cdot \rho \mathbf{r}}, \end{aligned} \quad (42)$$

$$\frac{\partial V_{loc}^l(\mathbf{g} = 0, z)}{\partial z_I} = -\frac{2\pi Z_I}{A} \operatorname{erf}(\sqrt{a}(z-z_I)). \quad (43)$$

Equation (37) and (38) imply

$$-ig_z V_{loc}^{at,s}(\mathbf{G}) = \frac{1}{L} \int dz e^{-ig_z z} \frac{dV_{loc}^s(\mathbf{g}, z)}{dz_I}, \quad (44)$$

and from this we can obtain the short-range part $\partial V_{loc}^s(\mathbf{g}, z)/\partial z_I$ by FFT. Then the force component in Eq. (17) was evaluated by

$$F_{Iz}^{loc} = -A_c \sum_{\mathbf{g}} \int dz n^*(\mathbf{g}, z) \left(\frac{\partial V_{loc}^l(\mathbf{g}, z)}{\partial z_I} + \frac{\partial V_{loc}^s(\mathbf{g}, z)}{\partial z_I} \right), \quad (45)$$

where A_c is the unit-cell area.

2. component due to the nonlocal potential

In the momentum space, Q_{nm}^{at} was expressed as

$$Q_{nm}^{at}(\mathbf{G}) = \int d\mathbf{r} e^{-i\mathbf{G} \cdot \mathbf{r}} Q_{nm}^{at}(\mathbf{r}) = \sum_{LM} C_{LM}^{l_n m_n, l_m m_m} \int d\mathbf{r} e^{-i\mathbf{G} \cdot \mathbf{r}} Q_{nm}^{at,L}(r) Y_{LM}(\hat{\mathbf{r}}). \quad (46)$$

Here, $C_{LM}^{l_n m_n, l_m m_m}$ is Clebsch-Gordan coefficient. In this work, we only consider the lowest angular moment [34]. Following the similar procedures given in Eqs. (36)-(38) and (44), we

get $\partial Q_{nm}^I(\mathbf{g}, z)/\partial z_I$. With these results, the integral in Eq. (18) was performed in \mathbf{g} -space to yield $F_{Iz}^{nl,1}$.

Next, it is clear that

$$\begin{aligned} & \langle \mathbf{k} + \mathbf{g}; j, \kappa | \frac{\partial \beta^I}{\partial z_I} \rangle \\ &= \frac{2\pi}{i^m} \sqrt{\frac{(2l+1)(l-m)!}{4\pi(l+m)!}} e^{-i(\mathbf{k}+\mathbf{g})\cdot\rho_{\mathbf{I}}} \int r^2 dr \sin\theta d\theta B'_{j,\kappa}(r \cos\theta + z_I) J_m(|\mathbf{k} + \mathbf{g}|r \sin\theta) P_l^m(\cos\theta) \beta(r) \end{aligned} \quad (47)$$

through Eq. (40). Consequently, we have $\langle \phi | \frac{\partial \beta^I}{\partial z_I} \rangle$ and $F_{Iz}^{nl,2}$ in Eq. (19) can be evaluated.

3. component due to NLCC

In a similar way for $\partial V_{loc}^s(\mathbf{g}, z)/\partial z_I$, we calculate $\partial n_c(\mathbf{g}, z)/\partial z_I$ to obtain

$$F_{Iz}^{nlcc} = -A_c \sum_{\mathbf{g}} \int dz v_{xc}^*(\mathbf{g}, z) \frac{\partial n_c^I(\mathbf{g}, z)}{\partial z_I}. \quad (48)$$

4. component due to the ion-ion interaction

For the 2D case, the \mathbf{g} -space part of the Ewald sum for E_{ii} with the auxiliary charge distribution

$$n_{\bar{a}}(\mathbf{r}) = \left(\frac{\bar{a}}{\pi}\right)^{3/2} Z e^{-\bar{a}|\mathbf{r}|^2} \quad (49)$$

is [60]

$$\begin{aligned} & E_{ii}^k \\ &= \frac{1}{A} \sum_{I \neq J} \left\{ \sum_{\mathbf{g} \neq \mathbf{0}} \frac{\pi Z_I Z_J}{|\mathbf{g}|} \left(e^{|\mathbf{g}||z_I - z_J|} \operatorname{erfc}\left(\sqrt{\bar{a}}\left(|z_I - z_J| + \frac{|\mathbf{g}|}{2\bar{a}}\right)\right) + e^{-|\mathbf{g}||z_I - z_J|} \operatorname{erfc}\left(\sqrt{\bar{a}}\left(-|z_I - z_J| + \frac{|\mathbf{g}|}{2\bar{a}}\right)\right) \right) \right. \\ & \quad \left. + Z_I Z_J \left(\pi |z_I - z_J| \operatorname{erf}\left(\sqrt{\bar{a}}|z_I - z_J|\right) + \sqrt{\pi/\bar{a}} e^{-\bar{a}|z_I - z_J|^2} \right) \right\} \cos(\mathbf{g} \cdot (\rho_{\mathbf{I}} - \rho_{\mathbf{J}})). \end{aligned} \quad (50)$$

After some algebra, the corresponding force is found to be

$$\begin{aligned} & F_{k,Iz}^{ii} \\ &= \frac{Z_I}{A} \sum_J \left\{ \sum_{\mathbf{g} \neq \mathbf{0}} \left[\pi Z_J \left(e^{|\mathbf{g}||z_I - z_J|} \operatorname{erfc}\left(\sqrt{\bar{a}}\left(|z_I - z_J| + \frac{|\mathbf{g}|}{2\bar{a}}\right)\right) - e^{-|\mathbf{g}||z_I - z_J|} \operatorname{erfc}\left(\sqrt{\bar{a}}\left(-|z_I - z_J| + \frac{|\mathbf{g}|}{2\bar{a}}\right)\right) \right) \right. \right. \\ & \quad \left. \left. + \frac{2\pi Z_J}{|\mathbf{g}|} \sqrt{\bar{a}/\pi} \left(e^{|\mathbf{g}||z_I - z_J|} e^{-\bar{a}\left(|z_I - z_J| + \frac{|\mathbf{g}|}{2\bar{a}}\right)^2} - e^{-|\mathbf{g}||z_I - z_J|} e^{-\bar{a}\left(-|z_I - z_J| + \frac{|\mathbf{g}|}{2\bar{a}}\right)^2} \right) \right] - 2\pi Z_I \operatorname{erf}\left(\sqrt{\bar{a}}|z_I - z_J|\right) \right\} \\ & \quad \times \cos(\mathbf{g} \cdot (\rho_{\mathbf{I}} - \rho_{\mathbf{J}})). \end{aligned} \quad (51)$$

For the sake of completeness, we write down the \mathbf{r} -space part of Ewald sum and its force component $F_{r,Iz}^{ii}$

$$E_{ii}^r = \frac{1}{2} \sum_{I \neq J} Z_I Z_J \frac{\text{erfc}(|\mathbf{R}_I - \mathbf{R}_J| \sqrt{\bar{a}})}{|\mathbf{R}_I - \mathbf{R}_J|}, \quad (52)$$

$$F_{r,Iz}^{ii} = -Z_I \sum_J Z_J \left(2\sqrt{\bar{a}/\pi} e^{-\bar{a}|\mathbf{R}_I - \mathbf{R}_J|^2} + \frac{\text{erfc}(|\mathbf{R}_I - \mathbf{R}_J| \sqrt{\bar{a}})}{|\mathbf{R}_I - \mathbf{R}_J|} \right) \frac{z_I - z_J}{|\mathbf{R}_I - \mathbf{R}_J|^2}. \quad (53)$$

In this work, we set \bar{a} in Eq. (49) equal to a in Eq. (32).

5. components due to the external E-field/Van der Waals interaction

When the system is influenced under an applied E-field, the associated force component is

$$F_{Iz}^E = -\frac{\partial E_E}{\partial z_I} = Z_I \mathcal{E}_0. \quad (54)$$

Moreover, if the Van der Waals interaction were taken into account, the DFT-D2 dispersion pair energy [54] of

$$E_{disp} = -\frac{1}{2} s_6 \sum_{I \neq J} \frac{C_{6,IJ}}{|\mathbf{R}_I - \mathbf{R}_J|^6} f(|\mathbf{R}_I - \mathbf{R}_J|) \quad (55)$$

with a damping factor

$$f_{IJ} = f(|\mathbf{R}_I - \mathbf{R}_J|) = \frac{1}{1 + e^{-d(|\mathbf{R}_I - \mathbf{R}_J|/R_{IJ}-1)}}, \quad (56)$$

is further added to the total energy. Note that the Ewald sum technique [61] is not implemented here. The parameters $s_6, C_{6,IJ}, R_{IJ}$ and d can be found in Ref. [54]. It can be easily shown that the z -component force due to this dispersion correction is given by

$$F_{Iz}^{disp} = -s_6 \sum_J C_{6,IJ} f_{IJ} \left[-f_{IJ} e^{-d(|\mathbf{R}_I - \mathbf{R}_J|/R_{IJ})} \frac{d}{R_{IJ}} + \frac{6}{|\mathbf{R}_I - \mathbf{R}_J|} \right] \frac{z_I - z_J}{|\mathbf{R}_I - \mathbf{R}_J|^7}. \quad (57)$$

The x - or y - components require no further comment. The details for these two components are described elsewhere [29, 30].

FIGURE CAPTIONS

Fig. 1: Total energy versus internal coordinate u of S in MoS₂ monolayer. The arrow indicates the energy minimum predicted by Broyden-Fletcher-Goldfarb-Shanno (BFGS) algorithm with $u = 0.4972$. See text for details.

Fig. 2: Band structure of (a) MoS₂ monolayer with a direct gap and (b) ZrS₂ monolayer with an indirect gap. (c) and (d) are the corresponding VASP counterparts.

Fig. 3: Band structure of charged graphene (a) without and (b) with charge neutrality condition by the present method. (c) Counterpart by VASP with charge neutrality condition.

Fig. 4: Convergence of the effective local potential during iteration for both electrically neutral and charged graphene.

Fig. 5: (a) Graphene bilayer with A-B stacking under an external E-field. (b) Non-uniform k -point sampling in surface Brillouin zone for the calculations in (a).

Fig. 6: Band structure of graphene bilayer near K under an external electric potential with various strengths. See text for details.

Fig. 7: (Color online) Screening charge density distribution of MoS₂ bilayer influenced by an external E-field. Thickness t defined as the distance between the center of gravity (CG) of the screening charge distribution of outermost charge layers [7].

FIG. 1:

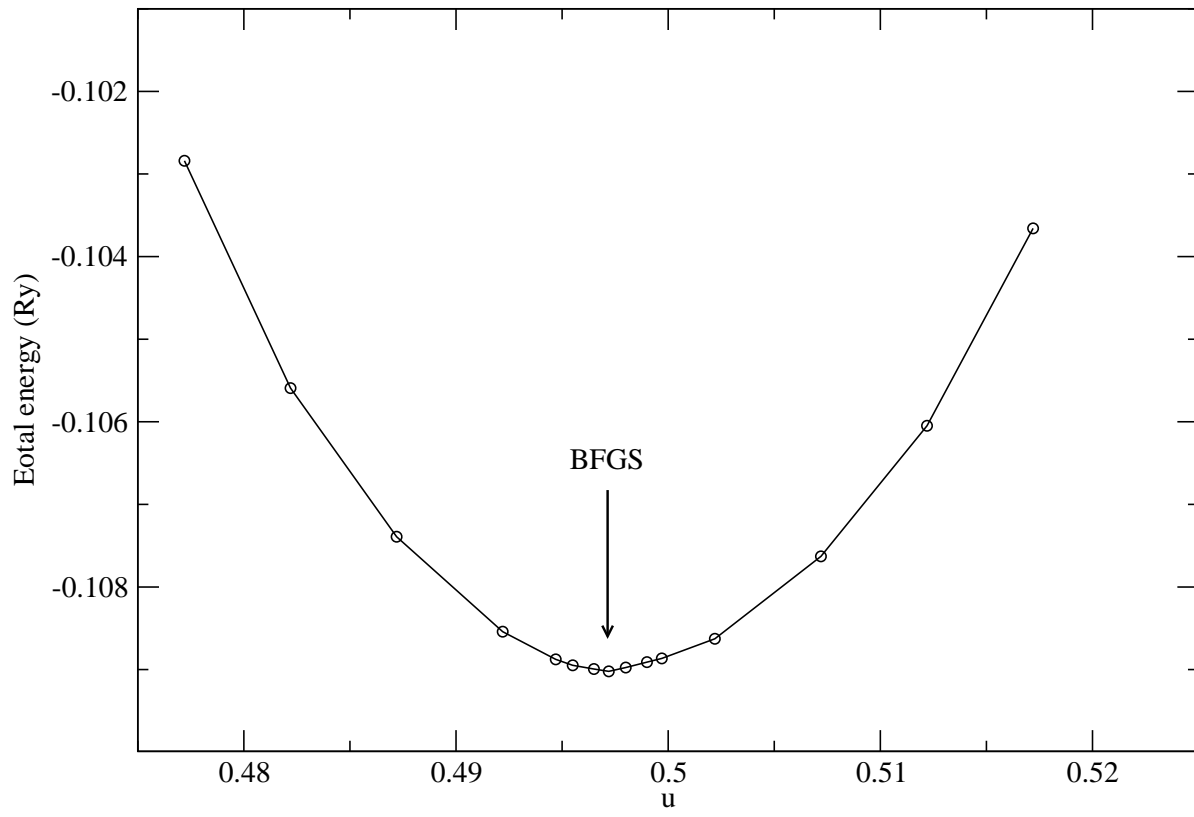


FIG. 2:

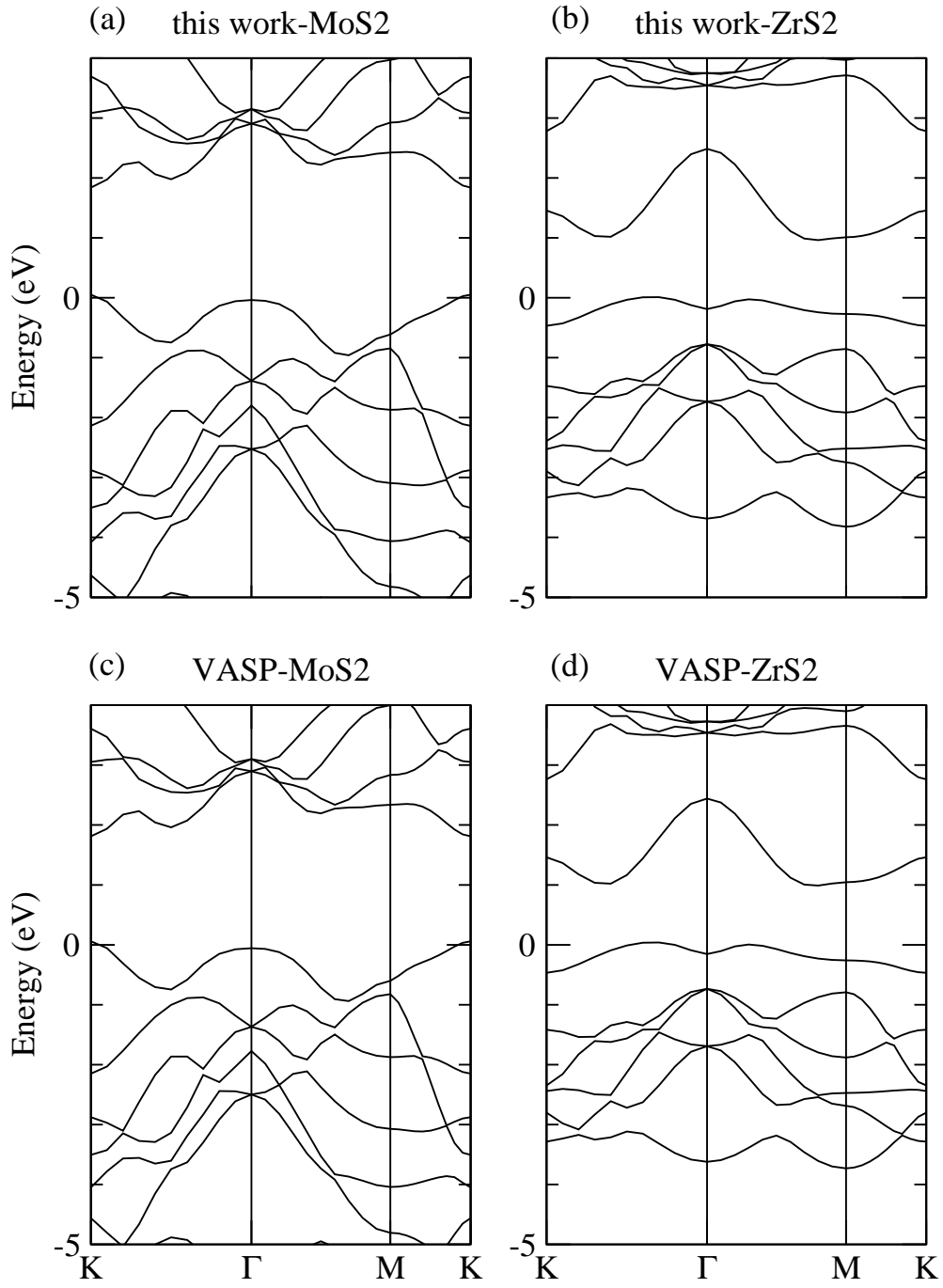


FIG. 3:

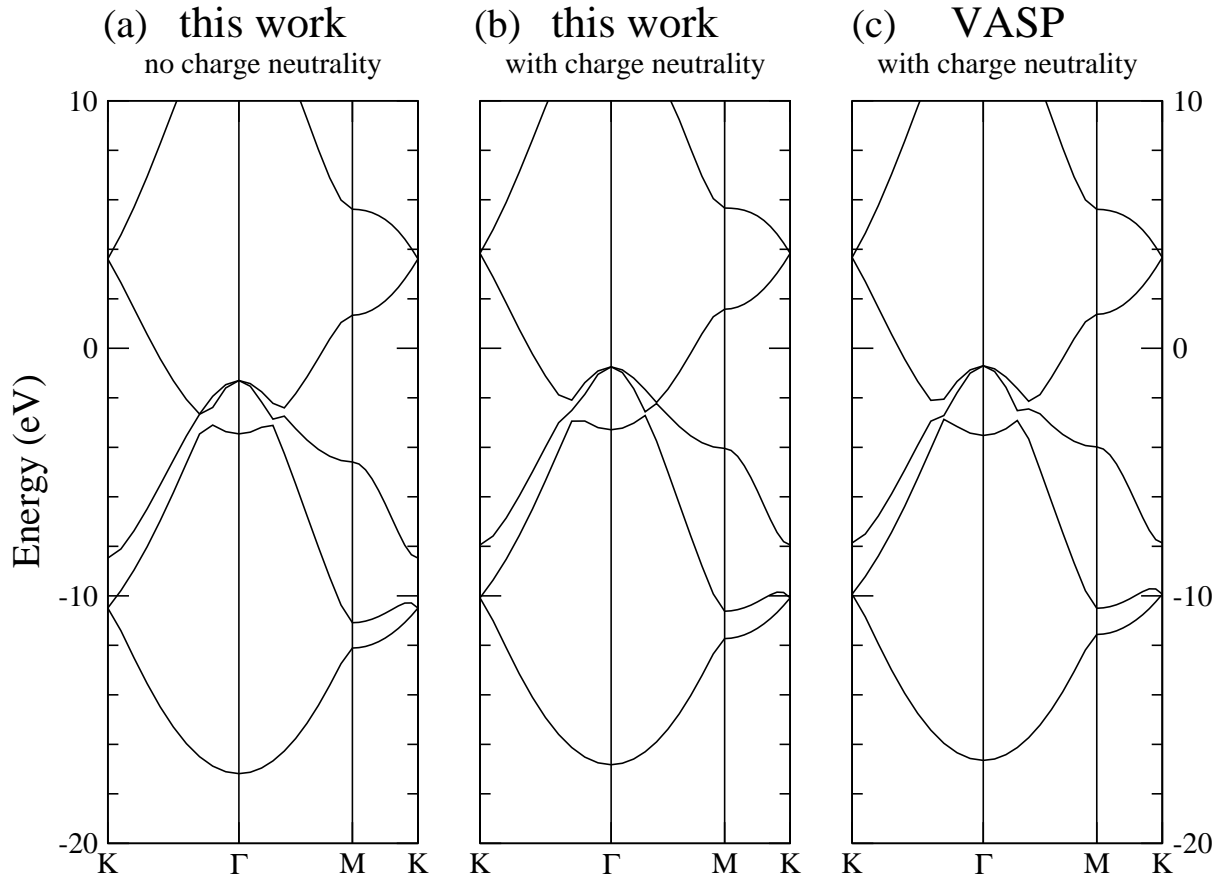


FIG. 4:

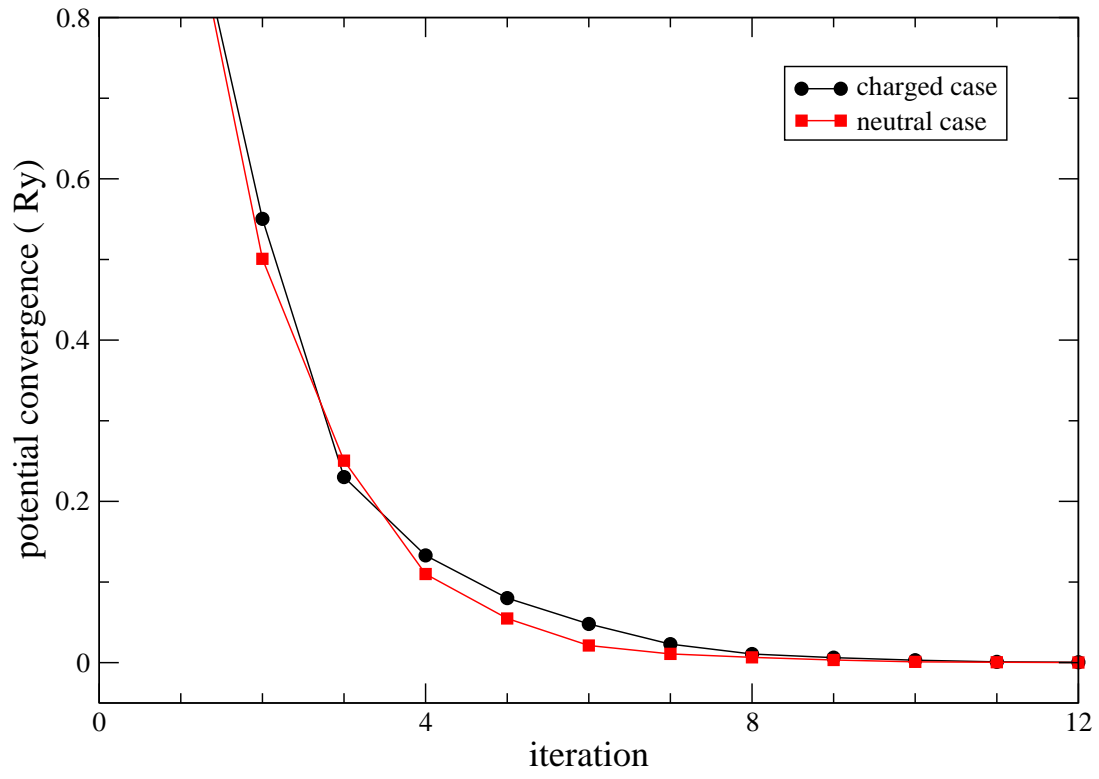
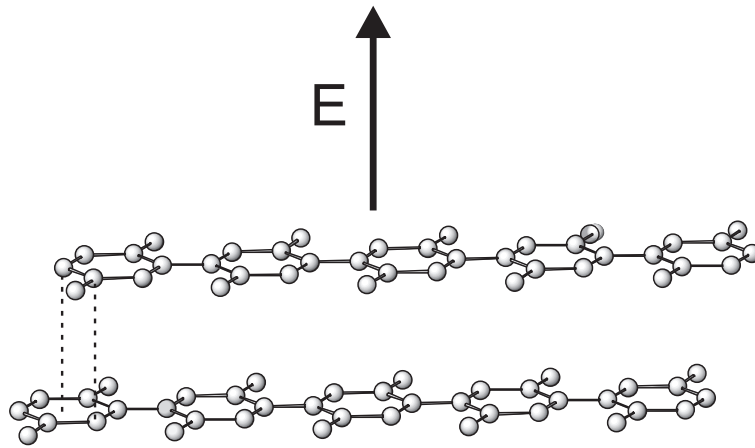


FIG. 5:

(a)



(b)

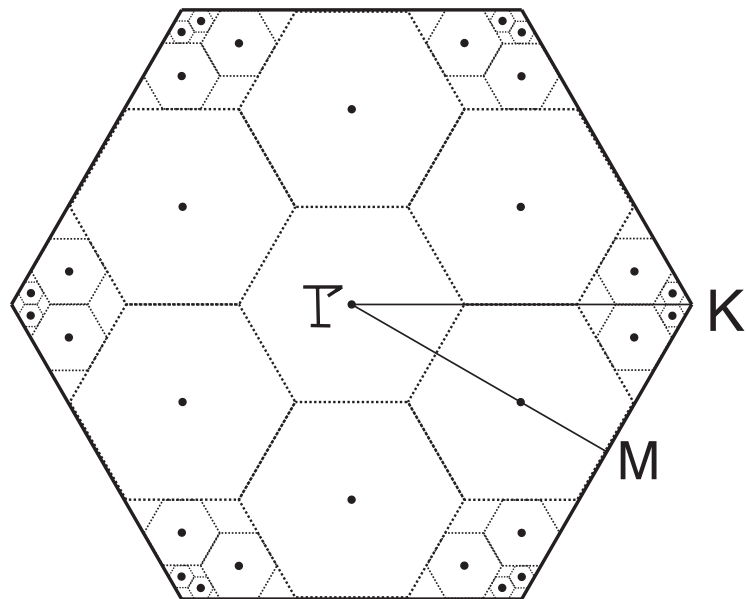


FIG. 6:

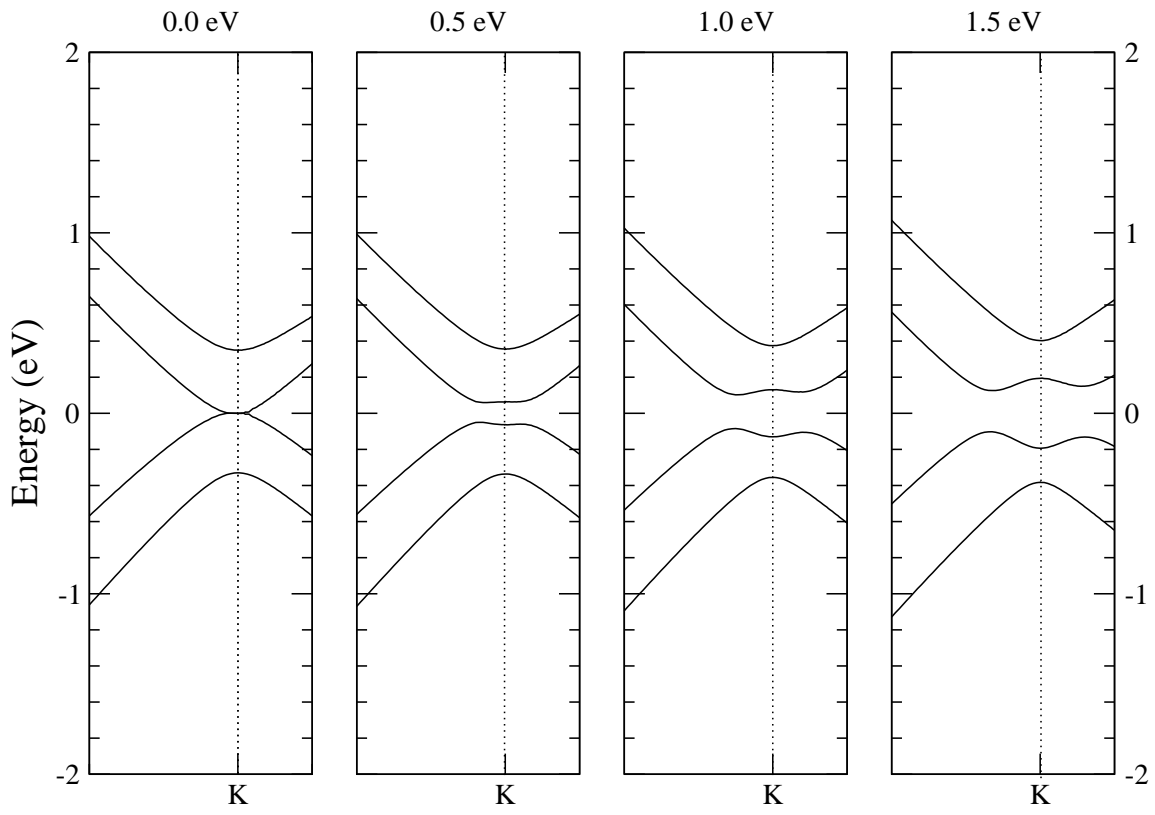


FIG. 7:

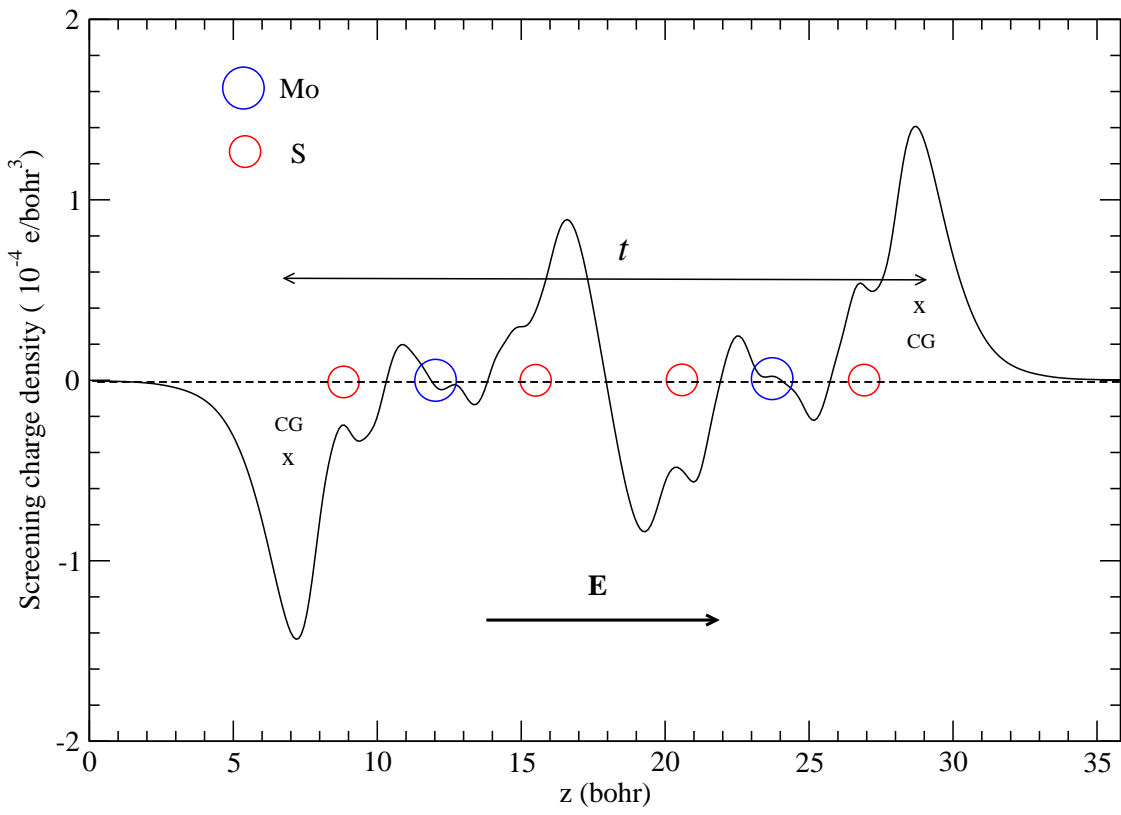


TABLE I: Relevant information for the total number of the wavefunction basis at point K used in MBA and VASP for monolayer MoS₂ and graphene (G). The data are produced based on lattice constant a_0 of 3.16 and 2.46 Å and energy cutoff of plane waves of 20 and 30 Ry for MoS₂ and graphene, respectively. The value labeled 'z-range' (Å) means the range where B-splines $B_{j,\kappa}$ are distributed. Two sets of c values (lattice constant along the perpendicular z direction, Å) with vacuum layer of 10 and 15 Å required in VASP are listed for comparison.

	MBA			VASP			
	z -range	$B_{j,\kappa}$ #	basis #	c	basis #	c	basis #
MoS ₂	12.64 ($4a_0$)	25	1100	13.16	1218	18.16	1662
G	8.00 ($3.25a_0$)	13	546	10.00	966	15.00	1422

TABLE II: The optimized vertical M-X distance d_z (Å) and band gap E_g (eV) in 2H MX₂ (M=Mo, W, Zr, Hf; X=S, Se) monolayer with experimental lattice constant a_0 (Å). VASP results are also shown for comparison.

	MoS ₂	WS ₂	MoSe ₂	WSe ₂	ZrS ₂	HfS ₂	ZrSe ₂	HfSe ₂
d_z	1.57	1.58	1.68	1.68	1.56	1.53	1.68	1.65
d_z (VASP)	1.57	1.59	1.68	1.70	1.56	1.54	1.68	1.66
E_g	1.79	1.97	1.58	1.68	0.95	0.96	0.81	0.82
E_g (VASP)	1.80	1.97	1.56	1.68	0.95	1.04	0.79	0.88
a_0 (exp)	3.16 ^a	3.15 ^b	3.28 ^c	3.28 ^d	3.66 ^e	3.63 ^f	3.75 ^g	3.77 ^h

^aRef. [37]

^bRef. [38]

^cRef. [39]

^dRef. [38]

^eRef. [38]

^fRef. [41]

^gRef. [40]

^hRef. [41]

TABLE III: The static out-of-plane dielectric constant ϵ_0 of monolayer (1L) and bilayer (2L) MoS₂ and ZrS₂ using various effective thickness t (a.u.). The dipole moment m multiplied by 4π ($\times 10^{-2}$ e/bohr²) is also listed. See text for details.

	$4\pi m$	t^a	ϵ_0	t^b	ϵ_0	ϵ_0^c
MoS ₂						
1L	4.86	11.57	6.3	9.97	38.9	6.4
2L	9.88	23.12	6.9	21.86	10.4	6.8
ZrS ₂						
1L	4.65	10.85	7.0	10.51	8.7	6.8
2L	9.31	21.66	7.1	23.12	5.1	6.9

^aRef. [55]

^bcalculated by following Ref. [7]

^cRef. [55]